



Numerical investigation of the scale effects of pump-jet propulsor with a pre-swirl stator

Downloaded from: <https://research.chalmers.se>, 2025-12-10 01:14 UTC

Citation for the original published paper (version of record):

Guo, C., Yang, C., Sun, C. et al (2023). Numerical investigation of the scale effects of pump-jet propulsor with a pre-swirl stator. *Physics of Fluids*, 35. <http://dx.doi.org/10.1063/5.0135604>

N.B. When citing this work, cite the original published paper.

Numerical investigation of the scale effects of pump-jet propulsor with a pre-swirl stator

Cite as: Phys. Fluids **35**, 027115 (2023); <https://doi.org/10.1063/5.0135604>

Submitted: 21 November 2022 • Accepted: 27 January 2023 • Published Online: 14 February 2023

 Chunyu Guo (郭春雨),  Chun Yang (杨春),  Cong Sun (孙聪), et al.



View Online



Export Citation



CrossMark

ARTICLES YOU MAY BE INTERESTED IN

[Numerical investigation of a propeller operating under different inflow conditions](#)

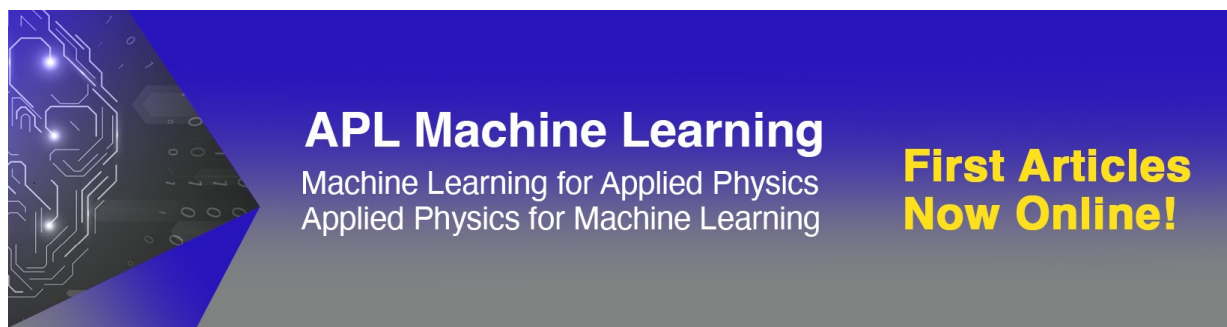
Physics of Fluids **34**, 105118 (2022); <https://doi.org/10.1063/5.0109801>

[Aeroacoustic control mechanism on near-wall-wing of Aero-train based on plasma jet](#)

Physics of Fluids **35**, 025122 (2023); <https://doi.org/10.1063/5.0136669>

[Propeller wake instabilities under turbulent-inflow conditions](#)

Physics of Fluids **34**, 085108 (2022); <https://doi.org/10.1063/5.0101977>



APL Machine Learning

Machine Learning for Applied Physics
Applied Physics for Machine Learning

**First Articles
Now Online!**

Numerical investigation of the scale effects of pump-jet propulsor with a pre-swirl stator

Cite as: Phys. Fluids **35**, 027115 (2023); doi: [10.1063/5.0135604](https://doi.org/10.1063/5.0135604)

Submitted: 21 November 2022 · Accepted: 27 January 2023 ·

Published Online: 14 February 2023



View Online



Export Citation



CrossMark

Chunyu Guo (郭春雨),¹ Chun Yang (杨春),² Cong Sun (孙聪),^{2,a)} Chao Wang (王超),² Huadong Yao (姚华栋),³ and Jianfeng Lin (林健峰)^{2,3}

AFFILIATIONS

¹Qingdao Innovation and Development Center of Harbin Engineering University, Qingdao 266000, Shandong, China

²College of Shipbuilding Engineering, Harbin Engineering University, Harbin 150001, China

³Department of Mechanics and Maritime Sciences, Chalmers University of Technology, Gothenburg 41296, Sweden

^{a)} Author to whom correspondence should be addressed: suncong@hrbeu.edu.cn

ABSTRACT

In this study, the performance of a pump-jet propulsor (PJP) with pre-swirl stator in open water is numerically investigated. Both full-scale and model-scale configurations are considered. The Reynolds-averaged Navier–Stokes equations and shear stress transport $k - \omega$ turbulence model are used in the numerical calculation. The computational domain is discretized using structured grids, and a rotating grid is affixed to the rotor to deal with the relative motion between the rotor and stationary components. The mesh quality is determined based on a grid uncertainty analysis. The numerical method is validated using model-scale experimental data. The simulation results reveal the influences of the scale size on the hydrodynamic performance and the distributions of the velocity, pressure and vorticity under three advance coefficients. With the increase in the advance coefficients, the scale influences on the efficiency become more obvious, and the efficiency of the full-scale PJP is always higher than that of the model-scale PJP. The full-scale configuration is found with a more significant instability in the gap vortex development, because it presents larger interaction between tip leakage vortex (TLV) and the inner wall of the duct. As the main velocity increases, the TLV shedding is delayed. Finally, the development process of gap vortices is analyzed for the difference operation conditions.

Published under an exclusive license by AIP Publishing. <https://doi.org/10.1063/5.0135604>

I. INTRODUCTION

The pump-jet propulsor (PJP) is a new type of propeller with lower noise and higher efficiency than a seven-blade highly skewed propeller. The duct can effectively muffle part of the radiated noise, and different forms of ducts can also improve the cavitation performance of the PJP. The stator consists of a pre-swirl stator and a front stator. The pre-swirl stator has a certain angle with the incoming flow, which makes incoming flow pre-swirl and makes stator's flow more uniform, thus improving the inflow conditions of the rotor. The front stator can recover the circumferential rotating wake of the rotor, which can effectively improve the propulsion efficiency of the PJP. PJPs are widely used in the shipbuilding industry.

Propeller performance is predicted using detached eddy simulation (DES) and Large Eddy Simulation (LES) methods by Wang *et al.*¹ They analyzed the instability of propeller wakes. The results show that the elliptical instability of each helicoidal tip vortex evolves into two interlaced spiral vortex branches under heavy loading conditions. The mutual inductance between neighboring tip vortices plays an important role in triggering the instability.² Shi *et al.*³ studied the wake dynamics

and destabilization mechanisms of four-blade propeller with and without duct based on modal decomposition technique and spectral analysis. The results show that underlying destabilization mechanisms in the wake correspond to some characteristic frequencies. The pairing of adjacent tip (leakage) vortices occurs at blade passing frequency (BPF). As studies of full-scale PJP tests are often too expensive, scale models are used. Experimental tests require considerable manpower and material and financial resources. In recent decades, with the rapid development of computer processing power, computational fluid dynamics (CFD) technology has become more mature and more reliable. Compared with experimental tests, CFD numerical simulation can greatly reduce the costs for the propeller performance analysis.

Numerous CFD studies of PJPs have focused on their hydrodynamic performance,^{4–6} cavitation performance,^{7,8} and noise performance.^{9,10} Li *et al.*^{11,12} studied the cavitation performance of PJP in a cavitation tunnel using the detached eddy simulation (DES) method and predicted the cavitation phenomenon of PJPs for different rotating speeds. The results showed that the cavitation of the blade increased the leakage of the upstream tip separation vortex and enhanced the

strength of the downstream tip leakage vortex (TLV). The interaction between the inflow turbulence and the tip vortices magnifies the instability motion of the tip vortex.¹³ Huang *et al.*¹⁴ analyzed the influence of duct parameters on the PJP flow field and found that increasing the duct length can effectively suppress the development of the tip leakage vortex but enhanced the trailing vortex of the stator blades. Qin *et al.*^{15,16} studied the problem of vortex instability in the wake of a PJP using the DES method and found that the unstable starting point of the tip vortex develops downstream as mainstream velocity increases. At a high advance coefficient, the stable length of the tip vortex decreases sharply. The influence of oblique flow on PJP was also analyzed,¹⁷ and the results showed that oblique flow had a great influence on the thrust performance of the rotor and duct. In addition, the influences of odd and even numbers of blades on the hydrodynamic performance and flow field of PJPs have been studied.¹⁸ Because of the unique structure of a PJP, the flow field at the clearance point is extremely complex. Lu *et al.*,¹⁹ Qiu *et al.*,²⁰ and Yu *et al.*²¹ studied the influence of different tip clearance heights on the hydrodynamic performance of PJP. The results show that the efficiency of the propulsor dropped more sharply with the increase in the tip clearance height. Using the potential flow method, Wang *et al.*^{22,23} analyzed the influence of gap flow on the hydrodynamic performance of PJPs. These studies were conducted on a model scale. In a full-scale PJP study, Shirazi *et al.*²⁴ showed that the stator produced a thrust that improved the overall PJP performance by 82%. Gong *et al.*²⁵ studied the wake dynamics of ducted propeller based on DES method. It is found that the blade-blade interference benefits the loading stability, the enhanced wake instability leads to the fast decline of the power spectral density peaks of kinetic energy at blade passing frequency and shaft frequency harmonics toward the far field under ducted conditions.

Previous studies of scale effects have focused heavily on conventional propellers and ducted propellers. Sun *et al.*²⁶ used the DES method to study scale effects for conventional propellers and found that the kinetic energy power spectral density of a full-size model was larger than that of a scale model. Abdel-Maksoud *et al.*²⁷ and Bhattacharyya *et al.*²⁸ compared the scale effects for a ducted propeller in numerical simulation and found that the duct thrust increased, and the rotor thrust decreased at full-size model. They also analyzed the hydrodynamic performance and scale effects of ducted propellers under different duct designs.^{29,30} The results show that all three ducts develop higher flow acceleration in full scale, causing an increase in the total induced velocity in front of the propeller and an increase in effectiveness. Choi *et al.*³¹ studied scale effects on pod propeller performance prediction and found a smaller resistance ratio of a pod propeller of full size. Yao and Zhang³² studied scale effects using a scale-model propeller and a full-size propeller. Their results show that the scale effect of propeller performance is mainly caused by different boundary layer flows. Yang *et al.*³³ conducted a numerical simulation of the cavitation hydrodynamics and low-frequency noise spectrum of three geometrically similar seven-blade highly skewed propellers and found that as the geometric dimensions increased, the propeller thrust coefficient increased and the torque coefficient decreased. Using the OpenFOAM software tool, Soydan and Bal³⁴ studied the influence of the scale effects on the hydrodynamic performance of a DTMB4119 propeller under conditions of cavitation and no cavitation. They found that as the geometric dimensions increased, the cavitation percentage increased.

A PJP is an extension of a ducted propeller. There have been few studies on scale effects for PJPs. Li *et al.*³⁵ conducted a numerical analysis of scale effects for PJPs and found that as the advance coefficient increases, the scale effect of the rotor is greater, the flow separation of the duct is weakened and the tip leakage vorticity increases, although it becomes more restricted as the advance coefficient increases. Yang *et al.*³⁶ studied the scale effects for PJPs using an internal solver and found that the change in the total thrust and torque coefficient was mainly contributed by the rotor.

The structure of the PJP is complex, and its scale effects have not been fully revealed. Few previous studies have studied the scale effects on hydrodynamic performance and gap flow. In the present work, the scale effects of full-scale and model-scale PJPs under different advance coefficients are comprehensively analyzed based on the unsteady Reynolds-averaged Navier–Stokes (URANS) method and the Shear Stress Transport (SST) $k - \omega$ turbulence model. The influence of the scale change on the evolution of gap vortices is studied.

II. NUMERICAL MODEL

A. Governing equations

In this paper, the single-phase flow is incompressible. In the numerical simulations, the unsteady Reynolds-averaged Navier–Stokes (URANS) equations are solved. The basic governing equations are the continuity equation and momentum equation,³⁷

$$\nabla \cdot \mathbf{U} = 0, \quad (1)$$

$$\rho \frac{\partial \mathbf{U}}{\partial t} + \rho \mathbf{U} \cdot \nabla (\mathbf{U}) = -\nabla p + \mathbf{F} + \mu \nabla^2 \mathbf{U}, \quad (2)$$

where \mathbf{U} is the flow velocity, consisting of the three directional components U_x , U_y , and U_z ; ρ is the density of the fluid (997.561 kg/m³); p is the flow field pressure; μ is the dynamic viscosity coefficient of the fluid (8.88871×10^{-4} Pa s); $\mu = \rho \cdot \nu$, and ν is the kinematic viscosity coefficient of the fluid (1.0×10^{-6} m²/s); and \mathbf{F} is the volume force.

Substituting the continuity equation [Eq. (1)] into the last part of the momentum equation [Eq. (2)] yields the following [Eq. (3)]:

$$\rho \frac{\partial \mathbf{U}}{\partial t} + \rho \mathbf{U} \cdot \nabla (\mathbf{U}) = -\nabla p + \mathbf{F} + \nabla B, \quad (3)$$

where B is a tensor related to the viscosity. Its components can be calculated using Eq. (4):

$$\tau_{ij} = \mu \left(\frac{\partial U_i}{\partial x_j} + \frac{\partial U_j}{\partial x_i} \right). \quad (4)$$

In this formula, x_i and x_j are spatial coordinate components and subscripts i and j take values of 1, 2, and 3.

Reynolds time-averaging is used to describe the instantaneous physical quantity as the sum of the time average and the instantaneous fluctuation value. The Reynolds-averaged velocity and pressure in the governing equations are time-averaged to obtain the time-averaged continuity equation and the URANS equation, whose component forms are as follows:

$$\frac{\partial \bar{U}_i}{\partial x_i} = 0, \quad (5)$$

$$\rho \frac{\partial \bar{U}_i}{\partial t} + \rho \frac{\partial (\bar{U}_j \bar{U}_i)}{\partial x_j} = -\frac{\partial \bar{p}}{\partial x_i} + f_i + \mu \frac{\partial}{\partial x_j} \left(\frac{\partial \bar{U}_i}{\partial x_j} - \rho \overline{U'_i U'_j} \right). \quad (6)$$

A term in the formula with a bar over it signifies the time mean of the term, and ' signifies the fluctuating value of a term. A term whose value is unknown, $-\rho \overline{U_i' U_j'}$, is introduced in the Reynolds-averaged Eq. (6). This unknown quantity mainly represents the Reynolds stress term in turbulence, and its physical meaning is the influence of the fluctuation phenomenon in turbulence on the mean flow. Because the number of unknowns in Eq. (6) is increased by nine, the equations are not closed. To make the equations solvable, it is necessary to make reasonable assumptions about the Reynolds stress term, $-\rho \overline{U_i' U_j'}$, establish the corresponding equation or add other turbulence equations, and then establish the conversion relationship between the pulsation value and the time mean value.

In this study, the commercial CFD software STAR-CCM+ is used as the viscous solver for numerical simulations. The pressure-velocity coupling is based on the SIMPLEC algorithm. A second-order upwind scheme is used for the convective term. A first-order implicit scheme is used for temporal discretization and five inner iterations are set for each time step.

B. Turbulence model

Many assumptions and calculation methods for the Reynolds stress term fall into two categories. One is represented by the Reynolds stress model, and the other is represented by the eddy viscosity model. The application of the eddy viscosity model is more extensive because when the eddy viscosity model is used to describe the turbulence, the Reynolds stress term is not calculated directly; rather, by adding the turbulent viscosity, the turbulent stress is expressed as a function of the turbulent viscosity. According to Boussinesq's assumption, the Reynolds stress of an incompressible flow can be expressed as follows:

$$-\rho \overline{U_i' U_j'} = \mu_t \left(\frac{\partial U_i}{\partial x_j} + \frac{\partial U_j}{\partial x_i} \right) - \frac{2}{3} \left(\rho k + \mu_t \frac{\partial U_i}{\partial x_i} \right) \delta_{ij}. \quad (7)$$

In Eq. (7), μ_t is the turbulent viscosity or eddy viscosity coefficient and δ_{ij} is the Kronecker symbol. The turbulence model can be a zero-equation model, a one-equation model, or a two-equation model, depending on the number of differential equations in μ_t . The most widely used are two-equation models, including the standard $k - \varepsilon$

model, the standard $k - \omega$ model, and an improved version of the two models.

In this paper, the most common SST $k - \omega$ turbulence model is used to close the equations. The model is a hybrid model proposed by Menter³⁸ in 1994 that combines the advantages of the $k - \omega$ model and the $k - \varepsilon$ model. A stable $k - \omega$ model is used near the wall, and the $k - \varepsilon$ model is used in the far field of the computational domain. The turbulence intensity equation k and turbulence frequency ω of the improved turbulence model are as follows:

$$\frac{\partial}{\partial t}(\rho k) + \frac{\partial}{\partial x_i}(\rho k U_i) = \frac{\partial}{\partial x_j} \left(\Gamma_k \frac{\partial k}{\partial x_j} \right) + G_k - Y_k + S_k, \quad (8)$$

$$\frac{\partial}{\partial t}(\rho \omega) + \frac{\partial}{\partial x_i}(\rho \omega U_i) = \frac{\partial}{\partial x_j} \left(\Gamma_\omega \frac{\partial \omega}{\partial x_j} \right) + G_\omega - Y_\omega + S_\omega, \quad (9)$$

where G_k and G_ω are turbulent kinetic energy production terms; Γ_k and Γ_ω are the diffusion rates of k and ω , respectively; Y_k and Y_ω are turbulent dissipation terms; and S_k and S_ω are source terms.

III. NUMERICAL VERIFICATION

A. Geometric model

In this paper, the research object is a pre-swirl stator PJP composed of thirteen pre-swirl stator blades, nine rotor blades, one duct, and one hub. A three-dimensional numerical model and experimental model of a PJP are shown in Fig. 1. Experimental model and experimental data (EFD) are from SSSRI (Shanghai Ship and Shipping Research Institute). The direction of incoming flow is the positive direction of the x axis, n is the rotational speed of the rotor, and the direction of rotation is clockwise. The inertial coordinate system $o - xyz$ is rotor's rotating coordinate system. The scale ratio is 1:3.5. The main parameters of the three-dimensional model of PJP are shown in Table I. The model-scale PJP is $\lambda = 3.5$, and the full-scale PJP is $\lambda = 1.0$. The diameter of the model-scale PJP is 204.85 mm, and the diameter of the full-scale PJP is 716.98 mm. The tip clearance between the rotor and the duct is 1 mm. The rotor speed of the model-scale PJP is 16 rps.

For the purposes of comparison and discussion of the numerical results, the hydrodynamic coefficients of PJP are non-dimensionalized.

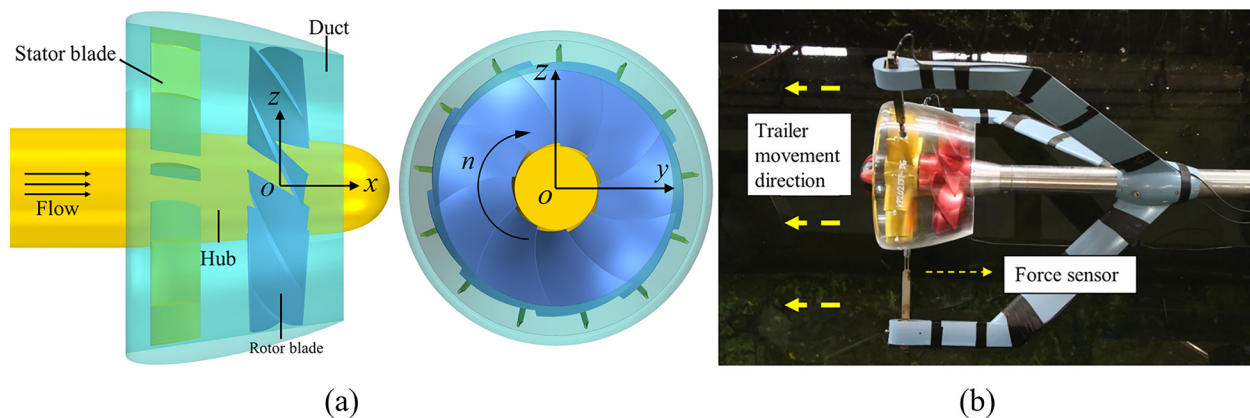


FIG. 1. Numerical model and experimental model. (a) Numerical model and (b) Experimental model.

TABLE I. Main parameters of PJP.

Parameter	Symbol	Full-scale PJP	Model-scale PJP
Scale ratio	λ	1	3.5
Number of stators	M	13	13
Number of rotors	N	9	9
Rotor diameter	D (mm)	716.98	204.85
Tip clearance	l (mm)	3.5	1
Revolution speed	n (rps)	8.55	16

The advance coefficient J , rotor thrust coefficient K_{Tr} , rotor torque coefficient K_{Qr} , stator thrust coefficient K_{Ts} , duct thrust coefficient K_{Td} , overall thrust coefficient K_T of PJP, and overall efficiency η_0 of PJP are defined as follows:

$$J = \frac{U}{nD}, \quad K_{Tr} = \frac{T_r}{\rho n^2 D^4}, \quad K_{Qr} = \frac{Q_r}{\rho n^2 D^5}, \quad K_{Ts} = \frac{T_s}{\rho n^2 D^4},$$

$$K_{Td} = \frac{T_d}{\rho n^2 D^4},$$

$$K_T = K_{Tr} + K_{Ts} + K_{Td}, \quad K_Q = K_{Qr}, \quad \eta_0 = \frac{J}{2\pi} \times \frac{K_T}{K_Q}, \quad C_p = \frac{p}{0.5\rho U^2},$$

where D is the diameter of the rotor, T_r and Q_r are the thrust and torque of the rotor, respectively; T_s is the stator thrust; and T_d is the duct thrust.

B. Computational domain and grid division

The computational domain of this article is illustrated in Fig. 2. The inlet boundary is set to $4D$ from the PJP, and the boundary condition is set to velocity inlet. The rotor speed was fixed in the numerical simulation, and the inlet velocity is adjusted according to the advance coefficient. The outlet is set to $7D$ from the PJP, and the boundary condition is set to pressure outlet. The influence of the computational domain size on the hydrodynamic performance of the propeller is studied as described by Baltazar *et al.*³⁹ The results show that the computational domain size has little effect on the hydrodynamic coefficient of the propeller. Therefore, in this paper, the computational domain cylinder diameter is $4D$, and the boundary condition is set to a no-slip wall. The rotating grid is affixed to the rotor to follow the rotation. The data interaction between the three sets of grids is carried out through the sliding interface.

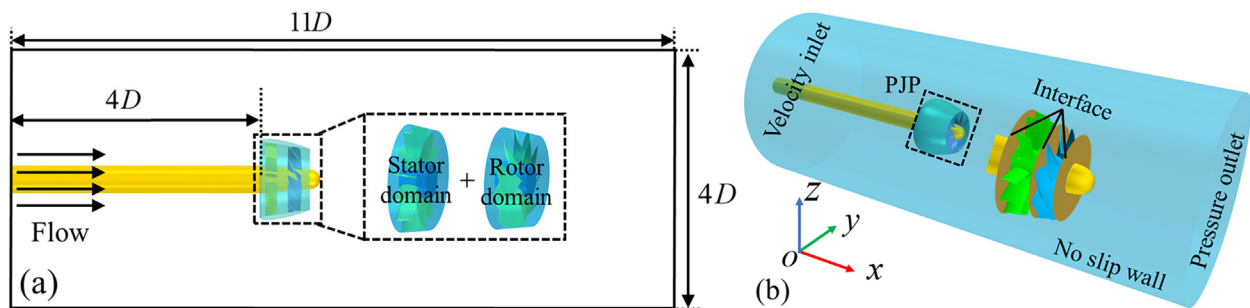


FIG. 2. Computational domain (a) and boundary condition settings (b).

Because of the complex structure of the PJP, the whole computational domain is divided into three domains in the numerical simulation: the rotor domain, containing the rotor blades; the stator domain, containing the stator blades; and external domain containing the rest of the PJP. The quality of the modeling of the complex flow field inside the PJP depends on the quality of the grid. To capture more details of the flow field inside the PJP, it is convenient to control the distribution of the grid nodes when meshing. Therefore, the ANSYS ICEM software is used to divide the structured hexahedral mesh. The rotor domain and stator domain are meshed using periodic meshing. First, a single rotor blade and stator blade are meshed, and the O-type topology is carried out near the blade. Then, the mesh of the whole rotor domain and stator domain is generated by periodic rotation.

There is a boundary layer in the PJP model, that is, there is a high-velocity gradient region in the flow field near the wall of the model. y^+ is a parameter that characterizes the internal structure of the boundary layer in terms of the dimensionless distance from the first grid to the model wall, which is related to shear stress, viscosity, and velocity. To solve the flow field details near the wall more accurately, it is necessary to set a reasonable y^+ value, as shown in Fig. 3. The y^+ value of the scale model is constrained to be within the range of 0–5. The first layer of the blade grid height is set to 8.0×10^{-6} m, and the spacing ratio is set to 1.2. The mesh of the model-scale PJP is enlarged by 3.5 times to obtain the mesh of the full-scale PJP. However, to reduce the mesh of the boundary layer region in the full-scale PJP, it was constrained to be between 30 and 350, so the mesh height of the first layer of the blade is set to 1.5×10^{-3} m, and the spacing ratio is set to 1.2. To capture the tip leakage vortex (TLV) in the internal flow field, 20 grid nodes are arranged at the gap. Details of the grid are shown in Figs. 4 and 5. In this paper, the Froude number Fr and the advance coefficient J between the model-scale PJP and the full-scale PJP are matched to calculate the rotation speed ($n = 8.55$ rps) of the full-scale PJP. Because the Reynolds number ($Re = [\rho C_{1.0R} \sqrt{U_\infty^2 + (\pi n D)^2}] / \mu$, where $C_{1.0R}$ is the chord length of the rotor blade at 1.0R) is different under two scale models, the height of the first boundary layer $[\Delta y = (y^+) C_{1.0R} \sqrt{74 Re^{-13/14}}]$ under two scale models is different, which explain why the boundary layers of two scale models are different.

C. Mesh uncertainty analysis

To assess the influence of mesh size on the numerical results for the hydrodynamic performance of the PJP, a mesh convergence

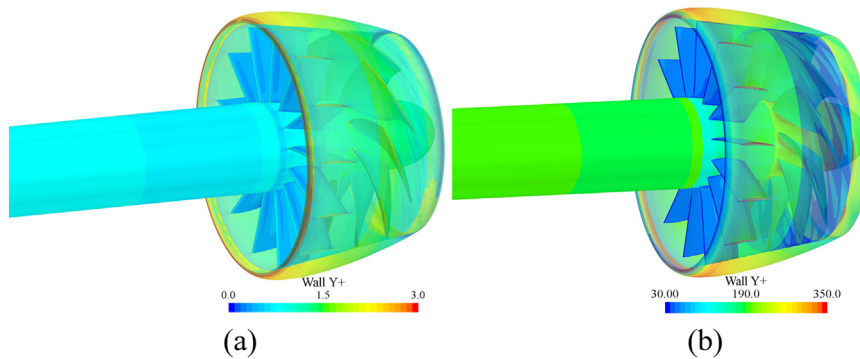


FIG. 3. Numerical model surface y^+ value. (a) Model-scale PJP and (b) Full-scale PJP.

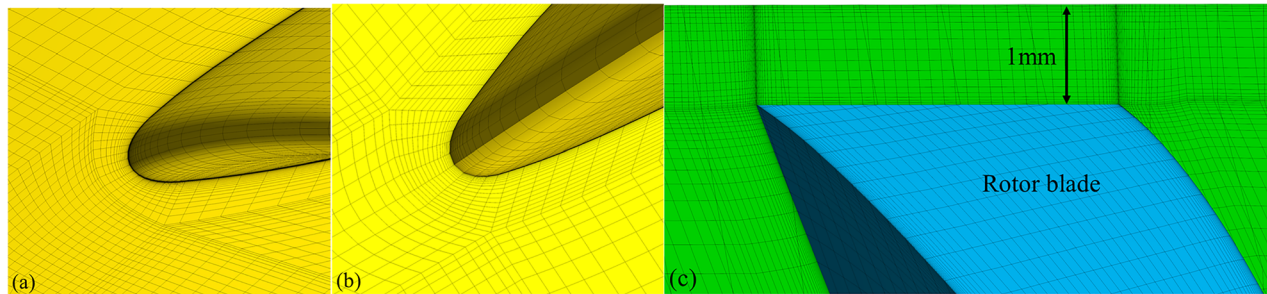


FIG. 4. PJP grid topology: (a) rotor blade boundary layer, (b) stator blade boundary layer, and (c) gap height.

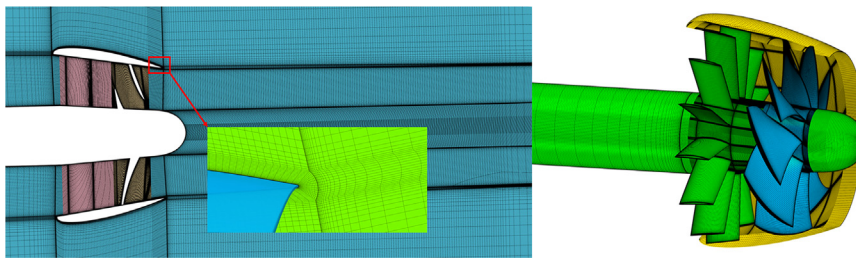


FIG. 5. Longitudinal section grid view.

analysis is carried out using the model-scale PJP under the conditions of advance coefficients of $J = 0.8$ and 1.1 and a velocity $n = 16$ rps. In the numerical calculation process, unsteady calculation is used. To satisfy the implicit scheme requirement (the Courant–Friedrichs–Lewy number: $CFL < 10$), the time step for present unsteady simulations was also set as 1.736×10^{-4} s, so that the rotor of model-scale PJP advanced 1° per step.⁴⁰ Numerical simulations were performed for ten rotor revolutions. Mesh generation is conducted according to the proportion of $\sqrt{2}$ to produce three different grid numbers consistent with three sets of grid topologies. The specific number of different grids is shown in Table II, and the grid diagram is shown in Fig. 6.

The mesh convergence rate is defined in the uncertainty analysis as follows:

$$R_G = \frac{S_1 - S_2}{S_2 - S_3}, \quad (10)$$

where S_i ($i = 1, 2, 3$) represents the results of K_{Tr} and K_{Qr} corresponding to the fine, medium, and coarse grids ID number. The convergence of the grid is judged according to the value of R_G . $|R_G| > 1$ represents

divergence, $-1 < R_G < 0$ represents oscillating convergence, and $0 < R_G < 1$ represents monotonic convergence.

The structural mesh refinement factor r is defined as $r = h_{coarse}/h_{fine}$. In this paper, r_{21} is 1.369 97, r_{32} is 1.456 98.

$$h = \left[\frac{1}{N_t} \sum_{i=1}^{N_t} \Delta_i \right]^{1/d}, \quad (11)$$

where N_t is the total number of grids and d is the number of calculation dimensions, which is three in this paper.

TABLE II. Three different sets of grids.

ID	Mesh	Rotor domain	Stator domain	External domain	Total
N_1	Fine	10.60×10^6	11.10×10^6	8.40×10^6	30.10×10^6
N_2	Medium	4.86×10^6	3.85×10^6	2.99×10^6	11.70×10^6
N_3	Coarse	1.45×10^6	1.35×10^6	0.99×10^6	3.79×10^6

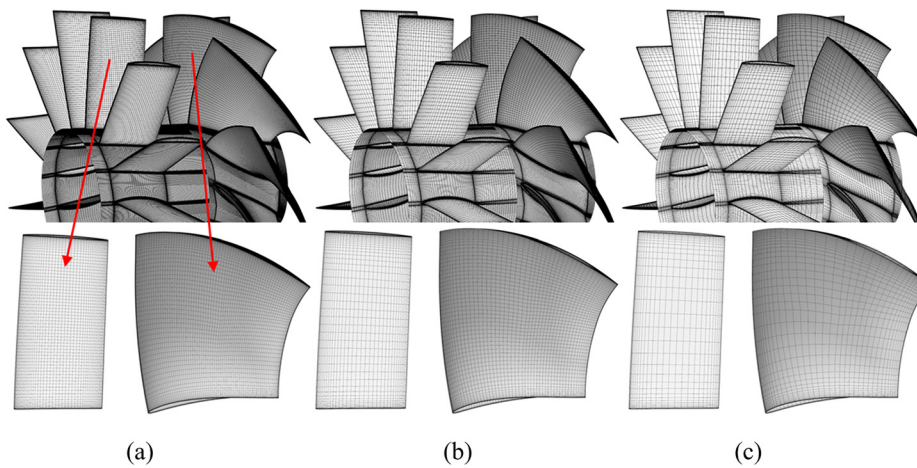


FIG. 6. The surface meshes with different resolutions. (a) Fine mesh (b) Medium mesh and (c) Coarse mesh.

Celik *et al.*⁴¹ defined the extrapolation value φ_{ext}^{21} , approximate relative error e_a^{21} , extrapolation relative error e_{ext}^{21} , and fine grid convergence index GCI_{Fine}^{21} :

$$C = \frac{1}{\ln(r_{21})} \left| \ln \left| \frac{S_1 - S_2}{S_2 - S_3} \right| + q(c) \right|, \quad (12)$$

$$q(c) = \ln \left(\frac{r_{21}^p - s}{r_{32}^p - s} \right), \quad s = 1 \cdot \text{sign} \left(\frac{S_1 - S_2}{S_2 - S_3} \right), \quad (13)$$

$$\varphi_{ext}^{21} = \frac{r_{21}^p S_1 - S_2}{r_{21}^p - 1}, \quad e_a^{21} = \left| \frac{S_1 - S_2}{S_1} \right|, \quad e_{ext}^{21} = \left| \frac{\varphi_{ext}^{21} - S_1}{\varphi_{ext}^{21}} \right|, \quad (14)$$

$$GCI_{Fine}^{21} = \frac{1.25 e_a^{21}}{r_{21}^p - 1}.$$

Tables III and IV show the results of numerical simulation and uncertainty analysis. For the two advance coefficients, the convergence rates of the thrust coefficient K_{Tr} and the torque coefficient K_{Qr} of the rotor are less than 1, so it is judged as monotonic convergence

TABLE III. Numerical simulation results.

ID	Mesh number	S_i	$J = 0.8$		$J = 1.1$	
			K_{Tr}	K_{Qr}	K_{Tr}	K_{Qr}
N_1	30.10×10^6	S_1	0.6582	1.5512	0.5706	1.3569
N_2	11.70×10^6	S_2	0.6560	1.5458	0.5670	1.3471
N_3	3.79×10^6	S_3	0.6515	1.5360	0.5626	1.3298

TABLE IV. Mesh uncertainty analysis.

		r_{21}	r_{32}	R_G	C	φ_{ext}^{21}	e_a^{21} (%)	e_{ext}^{21} (%)	GCI_{Fine}^{21} (%)
$J = 0.8$	K_{Tr}	1.369 97	1.456 98	0.489	3.212	0.6594	0.33	0.19	0.24
	K_{Qr}			0.551	2.775	1.5551	0.35	0.25	0.31
$J = 1.1$	K_{Tr}	1.369 97	1.456 98	0.820	1.347	0.5770	0.63	1.18	1.49
	K_{Qr}			0.570	2.674	1.3640	0.72	0.54	0.68

according to the formula. The maximum fine grid convergence index of the thrust coefficient is 1.49%, and the maximum torque coefficient is 0.68%. The value of GCI_{Fine}^{21} shows that increasing the number of grids does not greatly improve the hydrodynamic coefficient of the PJP. In addition, the contours of the wake field are roughly the same for different mesh numbers, but the dimensionless axial velocity changes, as indicated by the solid and dotted circles in the figure, and the wake of the PJP dissipates faster as the mesh number becomes larger. The results show that the grid division used in this paper is reasonable. To improve the quality of the flow field, the fine grid was selected for the subsequent calculation (Fig. 7).

D. Open-water performance verification of model-scale PJP

The open-water performance of the model-scale PJP is calculated using the fine grid, and compared with the experimental data from SSSRI, open-water simulation results are shown in Fig. 8. All data are the mean value of the last three rotor revolutions, as shown in Fig. 8(a). The results show that the variation trend of open-water performance curve of PJP is consistent with that of conventional propeller. The thrust coefficient K_{Tr} and torque coefficient K_{Qr} of the rotor decrease as the advance coefficient increases. The efficiency η_0 increases first and then decreases, and the advance coefficient value $J = 1.1$ is the best efficiency point. A comparison of the CFD calculation results and the experimental values shows that the errors of the rotor thrust coefficient K_{Tr} and the overall thrust coefficient K_T are below 4.5% and that the error of the rotor torque coefficient K_{Qr} is approximately 5%. The numerical simulation values are larger than

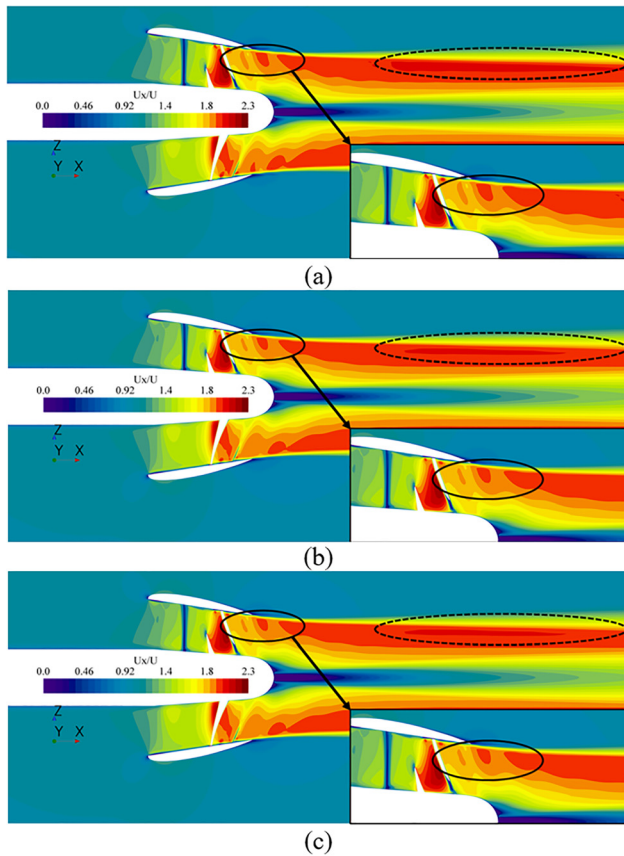


FIG. 7. Numerical results for instantaneous wake field at a time corresponding to ten rotor revolutions under the different grids ($J = 0.8$). (a) Fine mesh (b) Medium mesh and (c) Coarse mesh.

the experimental values, which may be due to the numerical simulation conditions being too idealized. The error in the overall efficiency η_0 is below -2.5% because the error in the rotor torque coefficient K_{Qr} is approximately 5% . Overall, the numerical results are in good agreement with the experimental values. This agreement suggests that the numerical and meshing methods used in this study are reasonable and can be used for subsequent calculations.

IV. NUMERICAL RESULTS AND DISCUSSION

A. Comparison of hydrodynamic coefficients

The heavy load condition ($J = 0.4$), the design condition ($J = 1.1$), and the light load condition ($J = 1.4$) are selected for analysis. To compare the differences between the force coefficients of the two models more conveniently, the differences were calculated using the formula $\Delta = 100\% \times (K_s - K_m)/K_m$, where K_s and K_m are the hydrodynamic coefficients of the full-scale PJP and model-scale PJP, respectively. The results for each coefficient are shown in Fig. 9.

When $J = 0.4$, the duct force is thrust, and the duct thrust coefficient of the full-scale PJP is larger than that for the model-scale PJP. As the advance coefficient increases, the duct force gradually becomes resistance, but the resistance coefficient of the model-scale PJP is larger than that of the full-scale PJP, because of the different degrees of

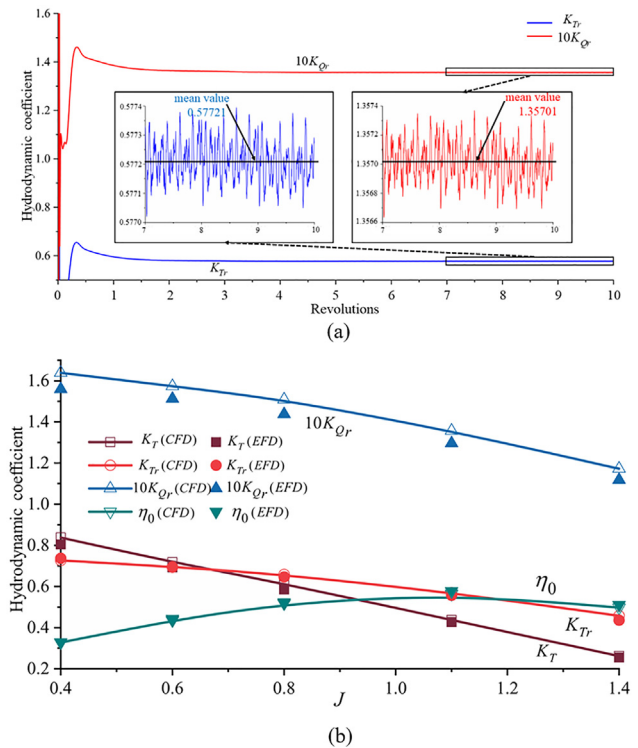


FIG. 8. Open-water simulation results for model-scale PJP. (a) The time histories of thrust coefficient K_{Tr} and torque coefficient $10K_{Qr}$ at $J = 1.1$ and (b) Numerical verification of open-water performance curve.

boundary layer separation between the leading edge and the trailing edge of the duct. The force of the stator in the two scale models is resistance. As the advance coefficient increases, the resistance coefficient decreases gradually, and the difference between the two scales remains small, but the resistance coefficient of the full-scale PJP is slightly smaller than that of the model-scale PJP. The thrust coefficient of the rotor is slightly larger for the full-scale PJP. The magnitude of the torque coefficient is related to the load, with that for the full-scale PJP being slightly smaller under a heavy load. However, under a light load, the torque coefficient of the full-scale PJP is slightly larger. The overall efficiency η_0 of the full-scale PJP is greater than that of the model-scale PJP. Because the scale effects have a greater impact on the duct, it makes the overall thrust coefficient larger for the full-scale PJP.

Figure 9 shows that the differences between the hydrodynamic coefficients are significantly different for different advance coefficients. The differences in the force coefficient of the duct are the largest. For $J = 0.4$, the difference in the duct is as high as 65.72% . As the advance coefficient increases, the difference decreases significantly. The differences in K_{Ts} , K_{Tr} , K_T , $10K_Q$, and η_0 increase as the advance coefficient increases. At a high advance coefficient, the efficiency difference of the full-scale PJP is 19.02% higher than that of the model-scale PJP.

B. Comparison of the velocity field

The scale effects of the PJP are analyzed in terms of instantaneous velocity fields, which are monitored at the time of ten rotor revolutions.

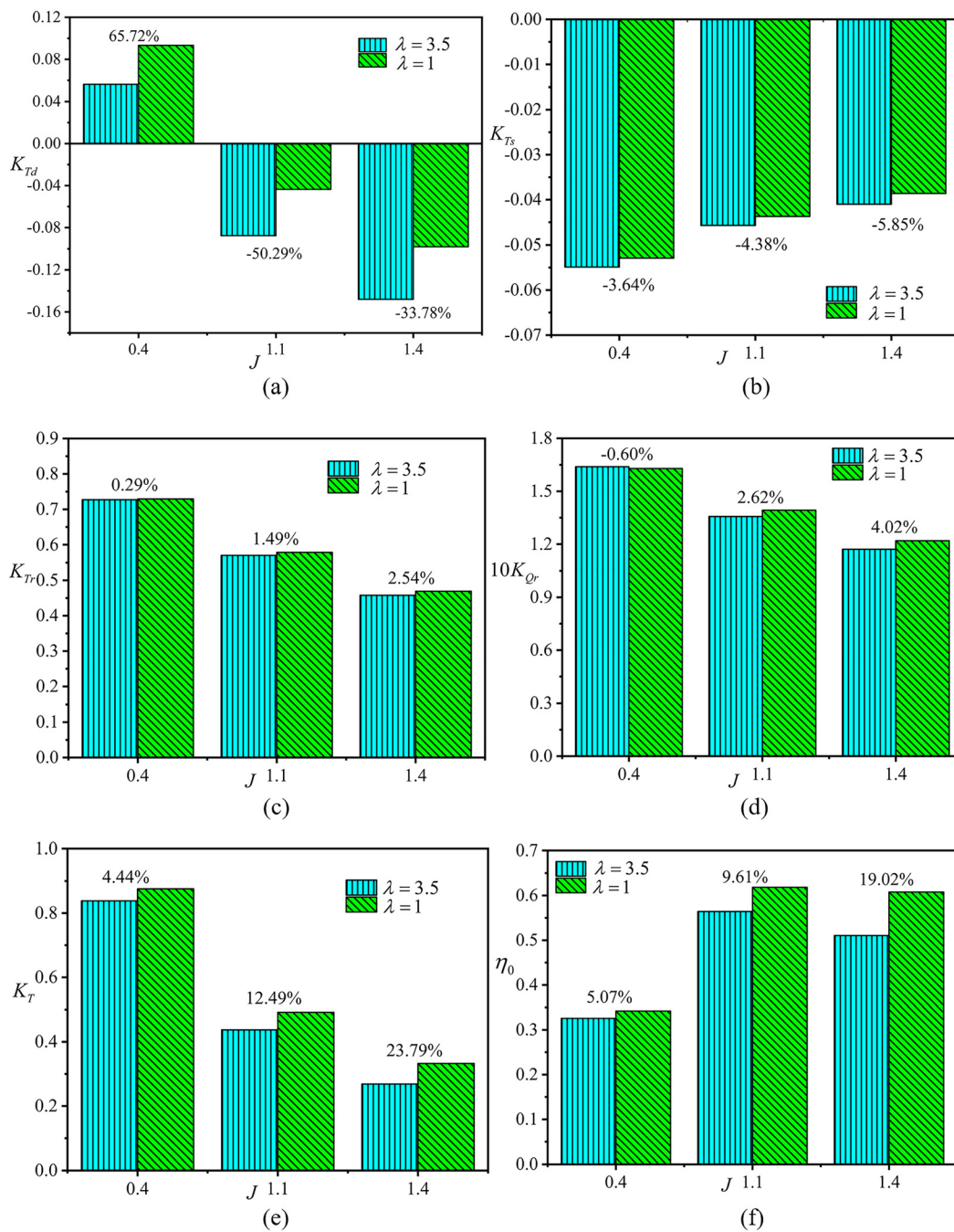


FIG. 9. Differences in hydrodynamic coefficients of the full-scale PJP and the model-scale PJP. (a) K_{Td} (b) K_{Ts} (c) K_{Tr} and (d) K_{Qr} .

Figure 10 shows the dimensionless axial velocity field comparison cloud map of the wake of the two scale models for different advance coefficients. Figure 10(a) shows the locations of the velocity monitoring points in the wake field. Figure 11 shows the dimensionless axial velocity comparison map of each monitoring point at two scales.

The wake field of the PJP is divided into three parts: the hub wake region, the core region, and the buffer region. The high-speed core region of the PJP wake shrinks inward during the downstream development at heavy load conditions, while the hub wake region and the buffer region expand outward. The velocity gradient in the axial direction of the buffer region and the hub wake region is large, and

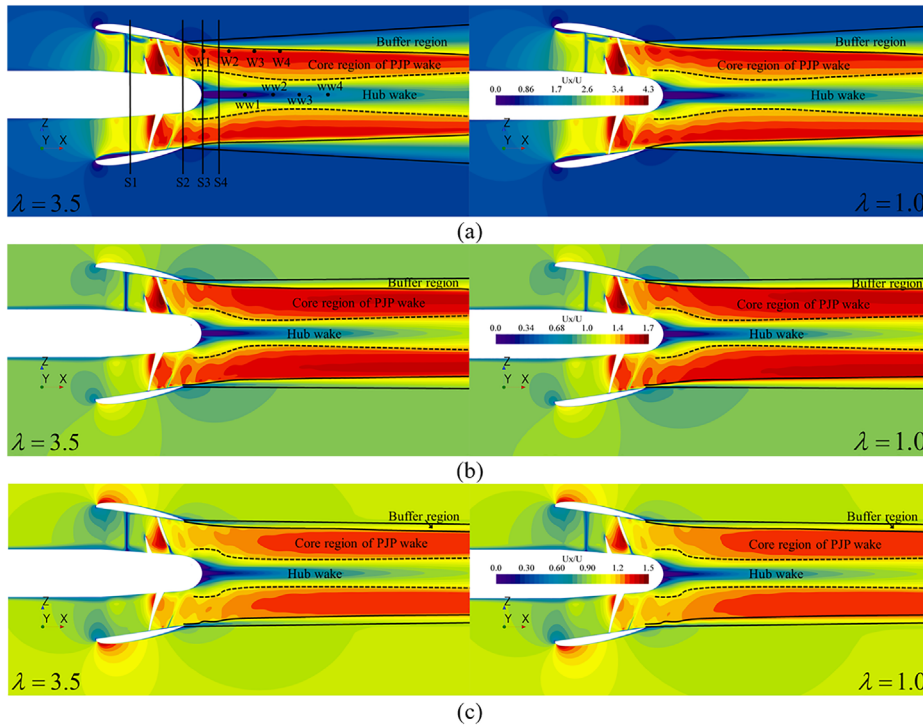


FIG. 10. Comparison of dimensionless velocity fields of two scale models at different advance coefficients (left: model-scale PJP and right: full-scale PJP). (a) $J = 0.4$ (b) $J = 1.1$ and (c) $J = 1.4$.

there is a large velocity difference with the high-speed core region, indicating that the flow disturbance between them and the high-speed core region flow is greater, so they have a significant deceleration effect on the high-speed core region, which makes the high-speed core region shrink significantly. In addition, as Fig. 11 shows the velocity values of the monitoring points of the model-scale PJP in the high-speed core area are smaller than those of the full-scale PJP, indicating that full-scale PJP rotor has a greater acceleration effect on the water flow in the high-speed core area, which also explains why the thrust coefficient of the full-scale PJP in Fig. 9 is slightly larger than that of

model-scale PJP. In addition, the velocity values of the monitoring points (ww1, ww2, ww3, and ww4) in the hub wake region for the full-scale PJP are larger, indicating that the velocity difference between the hub wake and the high-speed core flow is small and that its deceleration effect is small. The increase in the high-speed core flow and hub vortex velocity indicates that the wake field of the full-scale PJP tends to develop further. As the advance coefficient increases, the narrowing of the hub wake region and the buffer region reduces the influence of the deceleration effect on the high-speed core flow, which makes the high-speed core region gradually expand.

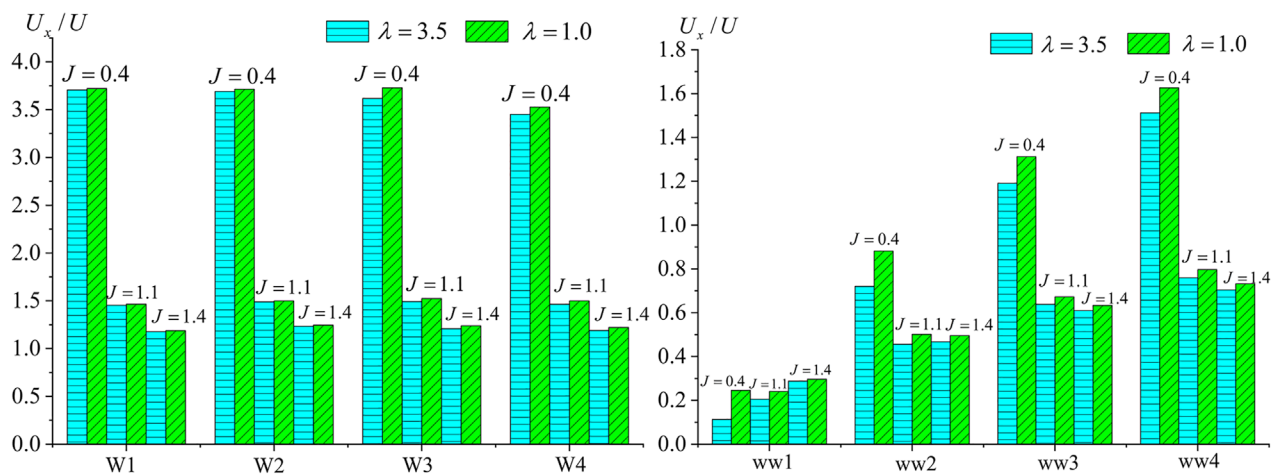


FIG. 11. Comparison of dimensionless axial velocities of monitoring points for different advance coefficients (left: W and right: ww).

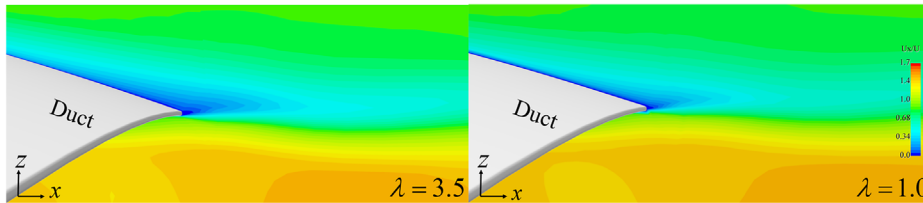


FIG. 12. Comparison of two scale models in dimensionless velocity field at the trailing edge of duct (left: model-scale PJP and right: full-scale PJP).

Figure 12 shows the velocity field of the trailing edge of the duct at the optimal efficiency point $J = 1.1$. The Reynolds number of the model-scale PJP is small, and the boundary layer separation of the trailing edge is more serious after the fluid passes through the duct, which means that the flow field behind the duct of the model-scale PJP is more disordered, which makes the duct shedding vortex more complicated.

The optimal efficiency point (advance coefficient $J = 1.1$) of the PJP is selected for the following analysis, and the flow field information for the four sections at $-0.2D_r$ in front of the rotor and $0.2D_r$, $0.4D_r$, and $0.6D_r$ behind the rotor (as shown in Fig. 10, S1, S2, S3, and S4) is intercepted. To compare the influence of scale effects, monitoring points are set at $0.8R$ on the corresponding section, and 18 monitoring points are established in the clockwise direction, with 12 clock points as 0° references and 20° intervals. Figure 13 shows the dimensionless axial velocity contours of the four sections, and Fig. 14 shows the axial velocity values of each monitoring point of the section.

The contours and curves show that for the full-scale PJP, the axial velocity amplitude of the wake is greater for the S2, S3, and S4 sections behind the rotor, which indicates that the acceleration of the water flow is enhanced during the rotor rotation. The suction effect on the incoming flow in front of the rotor is also enhanced, which makes the stator wake more uniform, especially the flow field near the stator hub (as indicated by the small black circles in Fig. 13), thereby improving the inflow conditions of the rotor. The increase in the velocity

amplitude of the stator flow field is equivalent to the stator working at lighter load conditions, which explains the decrease in the stator resistance coefficient shown in Fig. 9. In addition, for the flow field of the S3 section of the full-scale PJP, the increase in the amplitude of the hub wake velocity means that the influence of the deceleration effect in the hub wake region is reduced, and the high-speed core flow region develops further downstream, which is also verified by the S4 section velocity curve in Fig. 14 (S4).

Figure 15 shows the flow field cloud diagram of the PJP gap. The gap flow field structure during the high-speed rotation of the rotor is complex. The existence of the tip clearance causes the partial tip clearance fluid (TLF) to flow back from the pressure surface (PS) to the suction surface (SS), forming a tip leakage vortex (TLV). On the top of the blade tip, a part of the fluid also develops toward the rear of the blade tip, forming a tip separation vortex (TSV). In addition, the TLV interacts with the vortex on the inner wall of the duct to form an induced end wall vortex (IEV) during the development of the downstream.

Figure 16 shows the evolution path of the gap flow field vortex of the two scale models under three advance coefficients. To facilitate the observation of the motion law of the vortex at the gap from the guide edge to the end of the trailing edge, 14 sections were intercepted and numbered from 1 to 14. Combined with Fig. 15, the main flow velocity of the PJP is small at heavy load conditions ($J = 0.4$), the low-pressure center of the vortex leakage on the pressure surface of rotor

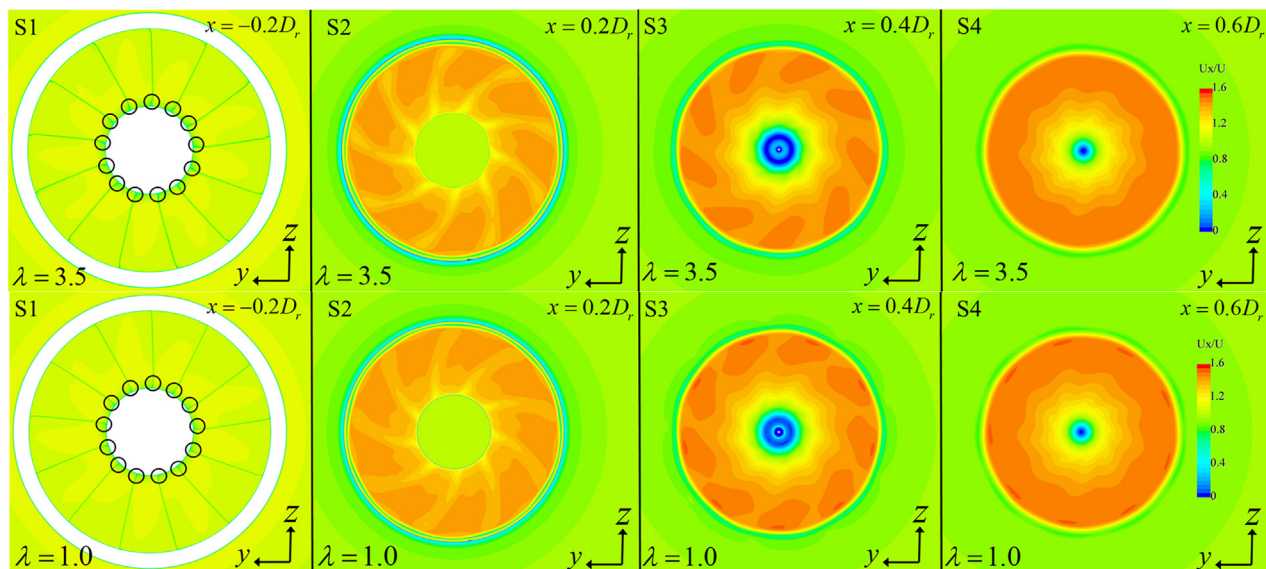


FIG. 13. Dimensionless axial velocity contours of four cross sections at $J = 1.1$ (top: model-scale PJP and bottom: full-scale PJP).

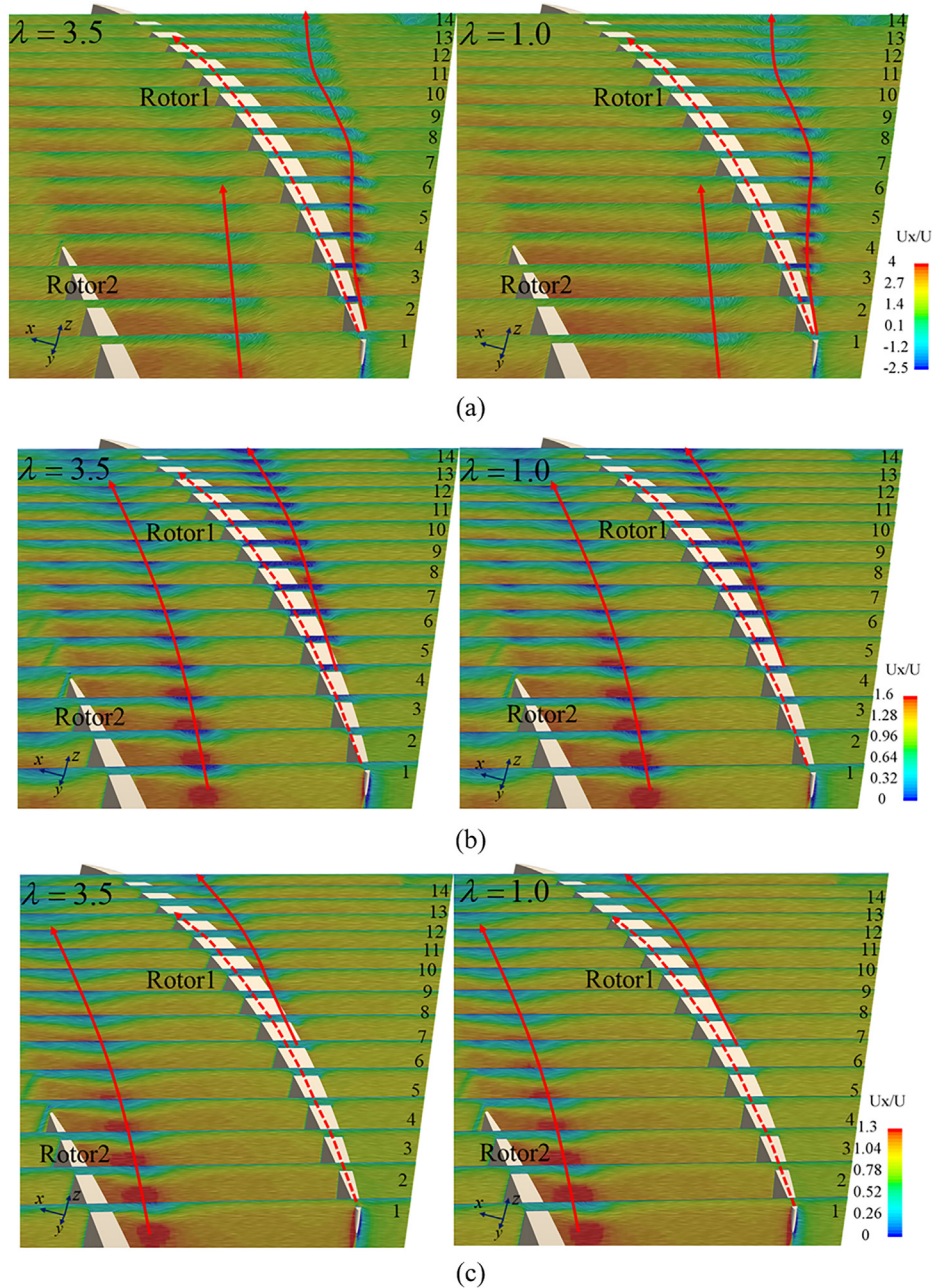


FIG. 16. Evolution path of the gap vortex for two scale models under different advance coefficients (left: model-scale PJP and right: full-scale PJP). (a) $J = 0.4$ (b) $J = 1.1$ and (c) $J = 1.4$.

mainstream velocity increases, the interaction between the TLV and the mainstream delays the TLV shedding.

To analyze the influence of the scale effects on the gap flow field, the optimal efficiency point $J = 1.1$ is selected. The contours of the gap vorticity x component in the $x - z$ plane for the two scale models is shown in Fig. 17. Overall, the evolution paths of the vortices under the two scale models are consistent. The TLV leaks from the pressure surface, and positive vorticity and negative vorticity develop downstream on the suction side. The TLV vorticity intensity of the model-scale PJP is larger, and the vortex intensity is

continuously dissipated during the downstream development of the TLV. The collapse phenomenon occurs at section 8, which makes the vorticity intensity of the vortex core center decrease rapidly. The TLV vorticity intensity of the full-scale PJP is smaller, and TLV collapses at section 7. In addition, because the TLV vorticity intensity of the full-scale PJP is smaller, the interaction with the inner wall vortex of the duct is weakened, which means that the vorticity intensity of the IEV for the full-scale PJP is also smaller than that of the model-scale PJP. As Fig. 18 shows, some of the fluid flows back from the gap to the suction surface, and some of the fluid continues

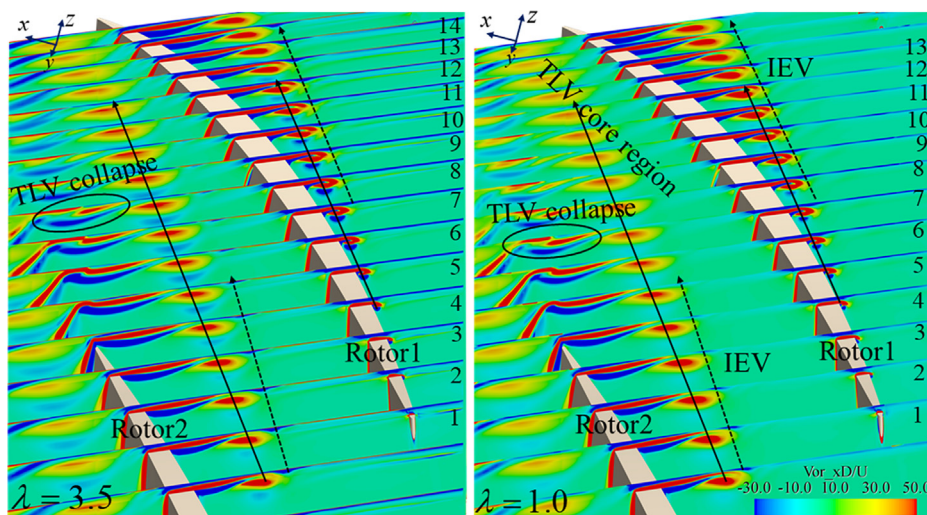


FIG. 17. Contour of x component of gap vorticity for two scale model $x-z$ planes at $J = 1.1$ (left: model-scale PJP and right: full-scale PJP).

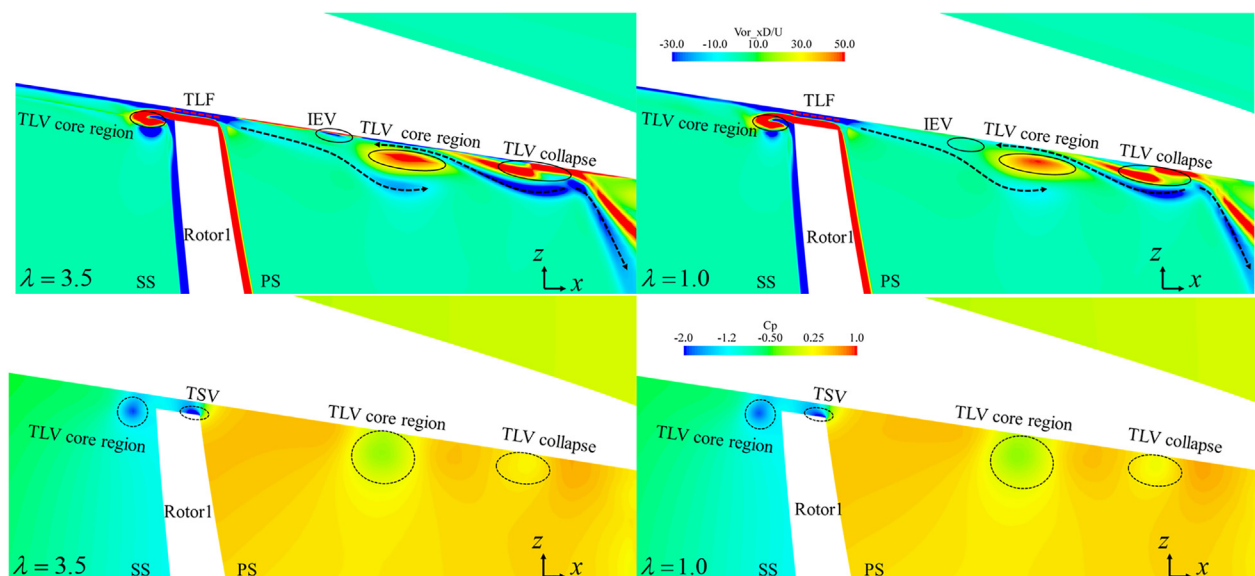


FIG. 18. Comparison of vorticity x component profile and pressure coefficient at section 7 for two scale models at $J = 1.1$ (left: model-scale PJP and right: full-scale PJP).

to flow along the main channel of the rotor and form a negative vortex below the TLV vortex core. The intensity of the positive and negative vortex of the full-scale PJP are smaller than those of the model-scale PJP. The TSV of the full-scale PJP is also smaller than that of model-scale PJP. The above analysis shows that the increase in scale size accelerates the instability of gap vortices. The evolution of the gap flow is shown in Fig. 19, which is similar to the gap flow vortex structure model of the axial pump described by Zhang *et al.*⁴²

C. Comparison of the pressure field

Figure 20 shows the pressure coefficient distribution of the longitudinal section and the duct trailing edge of the PJP. The results show that the duct flow field exhibits a strong scale effect. Because of the

difference in the Reynolds number, the boundary layer of the full-scale PJP becomes thinner, and the pressure coefficient at the leading edge of the duct is significantly lower at the full-scale PJP. The degree of flow separation at the trailing edge of the duct becomes smaller, which makes the pressure coefficient of the trailing edge of the duct higher (for example, the isoline of $C_p = 0.25$ on the surface of the trailing edge of the duct at full-scale PJP in Fig. 20). The pressure difference between the front and rear of the duct at full-scale PJP is larger than that of the model-scale PJP, which also explains the large difference in the force coefficient of the duct in Fig. 9. Because of the PJP gap, the pressure coefficient difference of the inner wall of the tube is mainly concentrated in the gap. As shown in Fig. 21, the negative pressure coefficients of the TSV and TLV for the model-scale PJP are larger, which means that the vorticity intensity is higher.

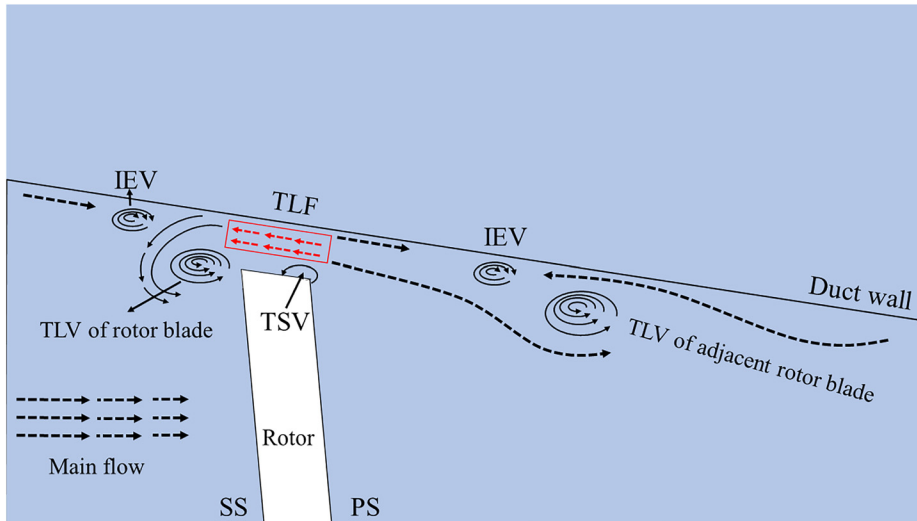


FIG. 19. Vortex structure model of gap flow field of PJP.

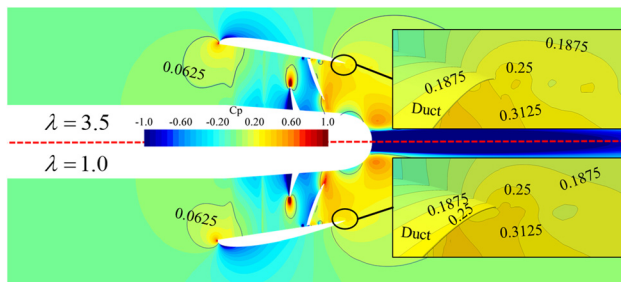


FIG. 20. Pressure distribution of middle longitudinal section and duct trailing edge at $J = 1.1$.

Figure 22 shows the pressure coefficient cloud diagrams of the stator and rotor blade surfaces. To compare the difference between the pressure surfaces and the suction surfaces of the blades more conveniently, the following formula is used to calculate the pressure coefficient difference: $C_{p1-diff} = (p_{ps} - p_{ss}) / 0.5\rho U^2$, where p_{ps} and p_{ss} represent the instantaneous pressures on the pressure surface and suction surface at a time corresponding to ten rotor revolutions. Three lines are intercepted on the stator and rotor blades, as shown in Fig. 22, and the difference curve is shown in Fig. 23. The stator and rotor suction surface pressures are greater than the pressure surfaces under the two models. For the pressure surface of the stator blade, the pressure coefficient of the model-scale PJP is slightly larger than that of the full-scale PJP. For the suction surface of the stator blade, the

pressure coefficient of the full-scale PJP much smaller than that of the model-scale PJP, because the suction effect of the rotor in the full-scale PJP improves the wake of the stator (Fig. 13). Similarly, the pressure coefficient for the full-scale PJP is smaller on the rotor pressure side, while the pressure coefficient is smaller than model-scale PJP on the suction side, because the improvement of the stator wake makes the inflow of the full-scale rotor more uniform. In addition, the figure shows that the pressure coefficient difference between the suction surface and the pressure surface is greater than that of model-scale PJP under three different sections.

To compare the fluctuating pressure changes near the rotor blade for the two scale models, four pressure coefficient monitoring points were set up in the radial direction of the rotor at 0.2D in front of the rotor, 0.2D after the rotor, and the gap (as shown in Fig. 24). The instantaneous pressure difference before and after the rotor is obtained using the pressure coefficient difference formula $C_{p2-diff} = (p_{di} - p_{rsi}) / 0.5\rho U^2$, where p_{di} and p_{rsi} represent the instantaneous pressure of the monitoring points at 0.2D before the rotor and 0.2D after the rotor, respectively.

The difference curves for each monitoring point are shown in Fig. 25. As the figure shows, the pressure coefficient difference between the front and back of the rotor blade is larger for the full-scale PJP, which explains why the rotor thrust coefficient is larger for the full-scale PJP. The fluctuating pressure coefficient of these monitoring points in the two periods after the flow field is stable. Because the rotor has nine blades, there are nine peaks and nine valleys in one rotation period of rotor, and there is $T/9$ (where T is the rotation period of the

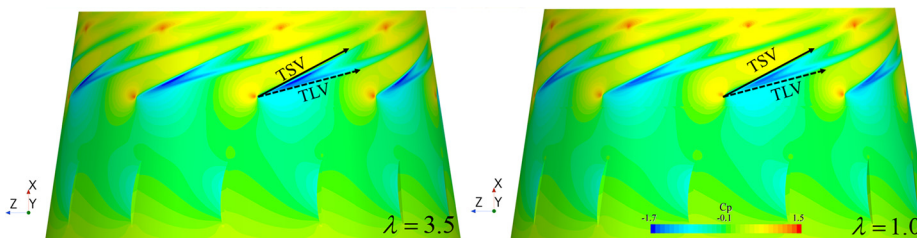


FIG. 21. Pressure coefficient distribution of inner wall of vessel at $J = 1.1$.

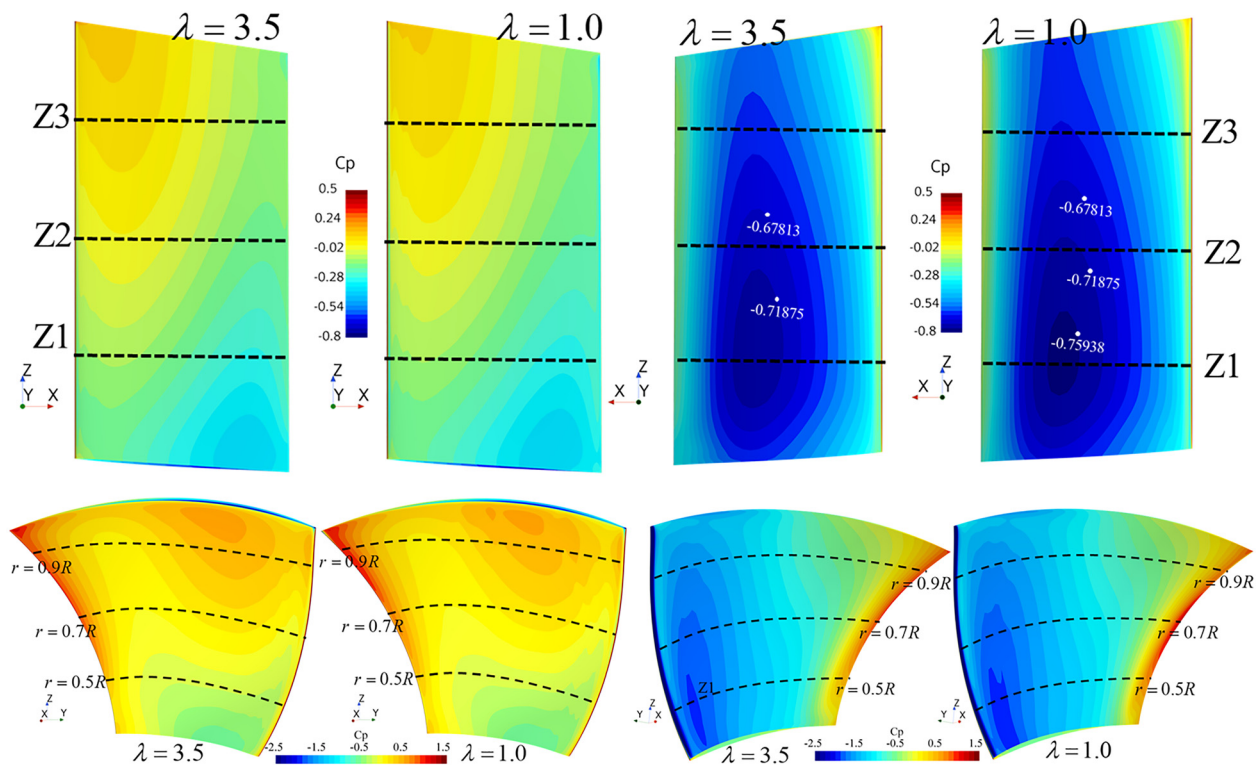


FIG. 22. Pressure coefficient distribution on blade surface (top: stator and bottom: rotor).

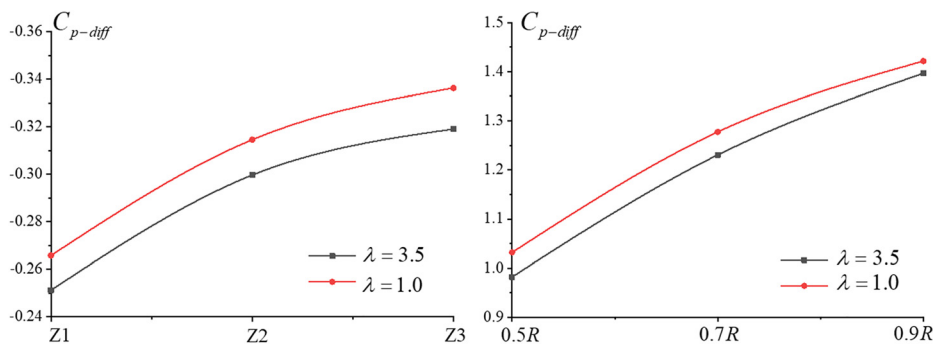


FIG. 23. Pressure difference curve of suction surface and pressure surface (left: stator and right: rotor).

rotor) between adjacent peaks. Because the rotation speed of the two models is different, the double-leaf frequency of the model-scale PJP is 144 Hz, and the BPF of the full-scale PJP is 76.95 Hz.

Figure 26 shows the time-domain and frequency-domain curves of the fluctuating pressure coefficient of the four monitoring points at 0.2D in front of the rotor. The time-domain curve under the two models is relatively smooth. The frequency-domain curve shows that the monitoring points in front of the rotor of the model-scale PJP have peaks at blade passing frequency (BPF) (144 Hz), 2BPF (288 Hz), and 3BPF (432 Hz). Similarly, the monitoring points of the full-scale PJP peak at BPF (76.95 Hz), 2BPF (153.9 Hz), and 3BPF (231 Hz). Since the rotor blades have a suction effect on the incoming flow, the BPF amplitude is large and can be ignored after 3BPF.

Figure 27 shows the time-domain and frequency-domain curves of the fluctuating pressure coefficients at four monitoring points 0.2D behind the rotor. After the water flow accelerates through the rotor, there is a certain radial and tangential velocity, and a certain degree of non-uniform wake occurs, resulting in a stronger fluctuating pressure behind the rotor. Therefore, it can be seen from the time-domain curve that the fluctuating pressure coefficient curves for the two models show different degrees of oscillation. Because the TLV vorticity intensity of the model-scale PJP is larger, the fluctuating pressure coefficient of the model-scale PJP oscillates more. It can be seen from the frequency-domain curves that the amplitudes of the fluctuating pressure for the two models are quite different. For the model-scale PJP, there are still fluctuating amplitudes after 3BPF. Although these

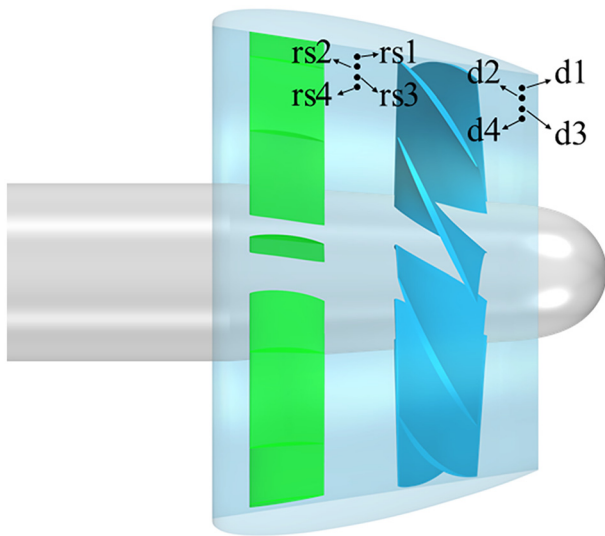


FIG. 24. Fluctuating pressure monitoring point setting.

amplitudes are negligible, the amplitude differences may increase as the scale ratio increases.

Figure 28 shows a comparison of the frequency-domain peak values of the fluctuating pressure coefficients at the monitoring points in front of and behind the rotor for the two scale models. Overall, the fluctuating peaks at the four monitoring points at 0.2D in front of the rotor are larger than those at the rear monitoring points. Because the TLV vorticity intensity on the pressure surface of the model-scale

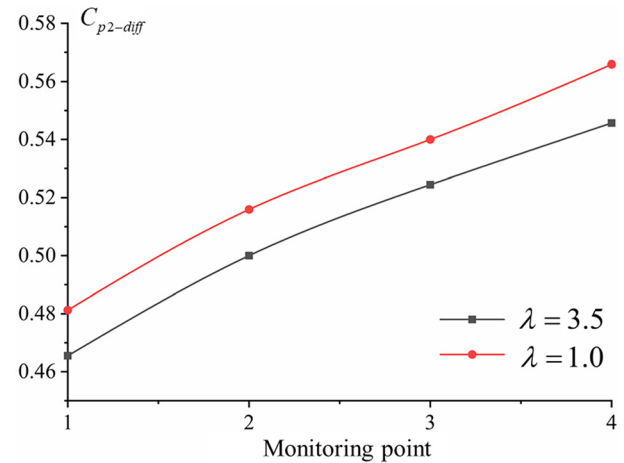
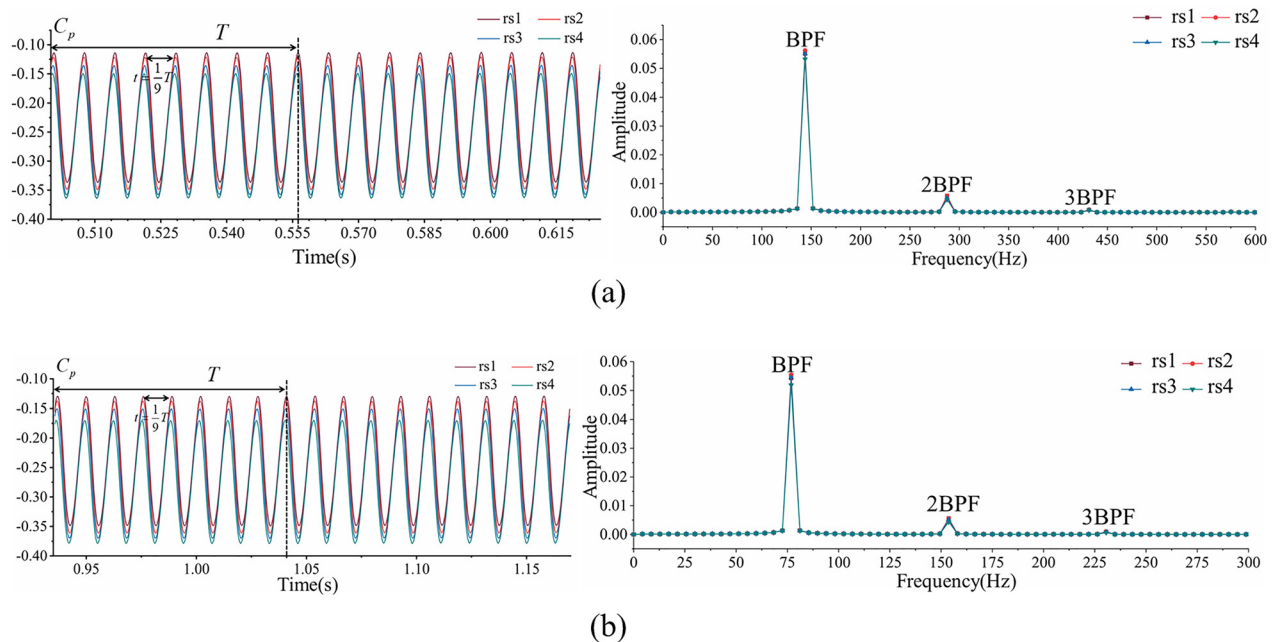


FIG. 25. Pressure coefficient difference comparison curves at 0.2D monitoring points before and after rotor for two scale models.

PJP is greater, the evolution of the TLV on the suction side produces a stronger fluctuating pressure on the front flow field. In addition, because the monitoring point rs2 is closest to the gap, the peak value of P_{rs2} in front of the rotor is the largest. The TLV continues to develop downstream. Among the four monitoring points at 0.2D behind the rotor, the peak value of the P_{d1} near the TLV vortex core is the largest, and the peak value of the P_{d4} near the hub is the smallest. Affected by the TLV vorticity intensity, the peak value of each monitoring point at the model-scale PJP is larger than that of the full-scale PJP.


 FIG. 26. Time-domain and frequency-domain curves of the fluctuating pressure coefficient at the monitoring point 0.2D before the rotor for the two models. (a) $\lambda = 3.5$ and (b) $\lambda = 1.0$.

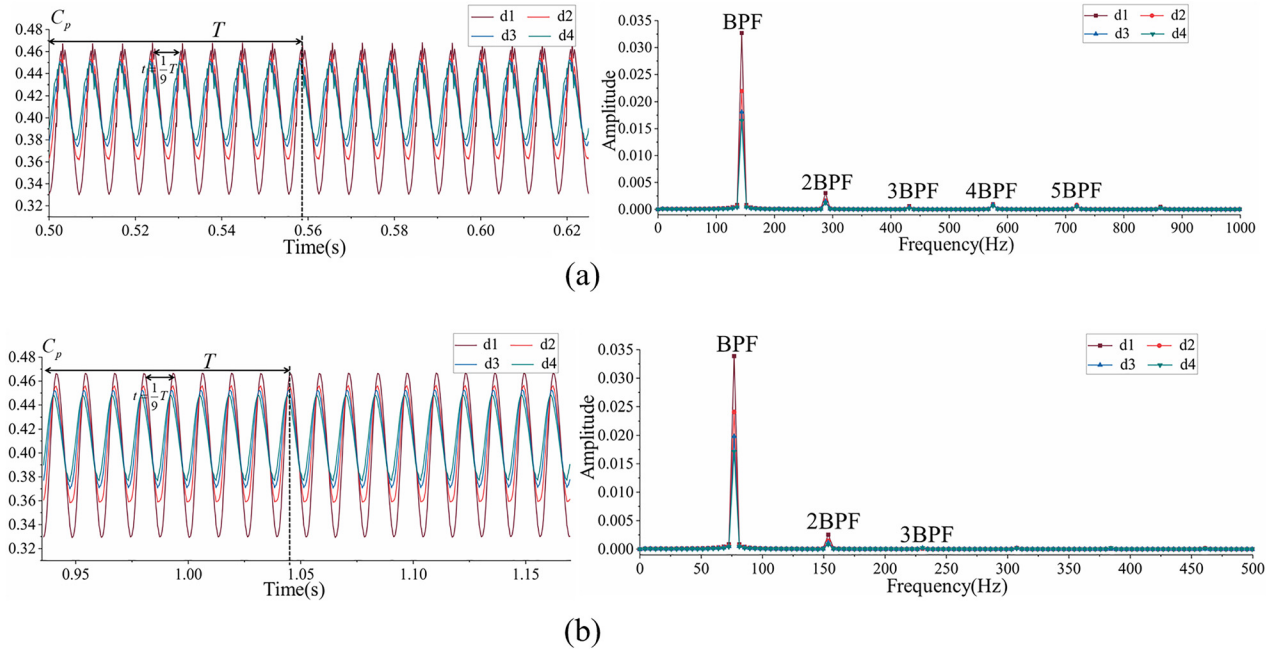


FIG. 27. Time-domain and frequency-domain curves of fluctuating pressure coefficient at 0.2D monitoring point after rotor for the two models. (a) $\lambda = 3.5$ and (b) $\lambda = 1.0$.

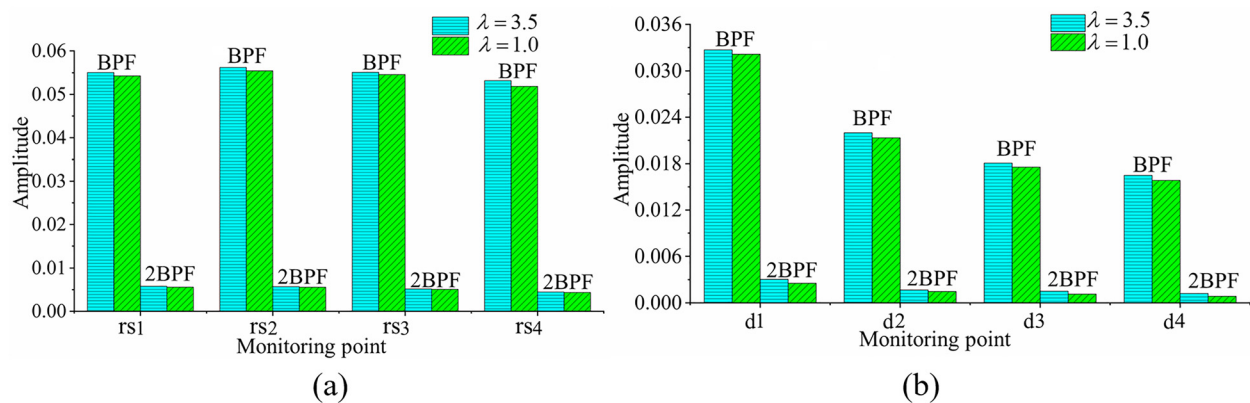


FIG. 28. Frequency-domain amplitude comparison of fluctuating pressure coefficients at monitoring points for the two models. (a) 0.2D ahead of rotor and (b) 0.2D rear of rotor.

V. CONCLUSION

In this paper, the scale effects on the flow near the PJP gap, which have not been fully revealed thus far, are numerically investigated using the URANS approach and SST $k - \omega$ turbulence model and verified based on open-water tests. By comparing the full-scale and model-scale PJPs at three advance ratios, the scale effects are addressed in terms of the hydrodynamic forces and the flow quantities, such as the vorticity and pressure.

In the model-scale and full-scale PJPs, K_{Tr} and K_{Qr} are less affected by the scale effects, and the most influential one is the duct force coefficient. Compared with model-scale PJP, the pressure coefficient difference between the front and rear rotor blades of the

full-scale PJP is greater, which makes K_{Tr} larger. K_{Qr} is mainly influenced by the load. The full-scale PJP has a lower K_{Qr} under heavy load conditions ($J = 0.4$), while the full-scale PJP has a higher K_{Qr} under light load conditions. In addition, the larger scale effect of the duct makes the K_{Tr} of the full-scale PJP higher, which indicates that η grows higher with the maximum efficiency difference of 19.02%. In addition, when the fluid flows through the duct, boundary layer separation occurs at the trailing edge of the duct. In the full-scale PJP, the separation phenomenon of the duct is weakened, which increases the pressure coefficient difference between the front and rear of the duct. Also, the increasing dimensionless axial velocity in the wake field of the full-scale PJP further explains the reason for the higher efficiency.

On account of the existence of the clearance, the vortices from the clearance include TLF, TLV, TSV, and IEV. Among them, the TLV released from PS continues downstream at SS. With the advance coefficient increases, the mainstream velocity gets higher, the leakage position of TLV at the top of the blade slowly moves backward, and the angle between TLV and the corresponding blade gradually becomes smaller. The full-scale configuration is found with a more significant instability in the gap vortex development. Compared with the model-scale PJP, the TLV vorticity intensity of the full-scale PJP is weaker, the vortex collapses earlier (TLV collapses at section 7), and the interaction with the duct wall vortex is weakened, which lowers the intensity of IEV vorticity. Additionally, in the full-scale PJP, both the negative pressure coefficient of the TSV at the top and the frequency domain peak of fluctuating pressure in the gap flow field are smaller than that of the model-scale PJP. Finally, the development process of gap vortices is obtained.

The present study is limited to the use of URANS for the numerical simulations. A future work will be to adopt DES or LES to explore the flow field at the gap more deeply, and a larger scale model can be considered.

ACKNOWLEDGMENTS

This work was financially supported by the Natural Science Foundation of Heilongjiang Province (Grant No. LH2021E042) and Fundamental Research Funds for the Central Universities (Grant No. GK2010260353).

AUTHOR DECLARATIONS

Conflict of Interest

The authors have no conflicts to disclose.

Author Contributions

All authors contributed to the study conception and design. Mesh division and numerical simulation, data collection, and analysis were performed by Chun Yang. The first draft of the manuscript was written by Chun Yang and all authors commented on previous versions of the manuscript. Chun-Yu Guo revised it critically for important intellectual content. Cong Sun, Chao Wang, Hua-Dong Yao, and Jian-Feng Lin helped perform the analysis with constructive discussions. All authors read and approved the final manuscript.

Chunyu Guo: Software (equal); Writing – review & editing (equal). **Chun Yang:** Data curation (equal); Formal analysis (equal); Validation (equal); Writing – original draft (equal). **Cong Sun:** Project administration (equal); Writing – review & editing (equal). **Chao Wang:** Supervision (equal); Writing – review & editing (equal). **Hua-Dong Yao:** Supervision (equal); Writing – review & editing (equal). **Jianfeng Lin:** Writing – review & editing (equal).

DATA AVAILABILITY

The data that support the findings of this study are available from the corresponding author upon reasonable request.

REFERENCES

- ¹L. Wang, T. Wu, J. Gong, and Y. Yang, “Numerical simulation of the wake instabilities of a propeller,” *Phys. Fluids* **33**, 125125 (2021).

- ²L. Wang, X. Lu, and T. Wu, “Modal analysis of the propeller wake under the heavy loading condition,” *Phys. Fluids* **34**, 055107 (2022).
- ³H. Shi, T. Wang, M. Zhao, and Q. Zhang, “Modal analysis of non-ducted and ducted propeller wake under axis flow,” *Phys. Fluids* **34**, 055128 (2022).
- ⁴C. Qiu, G. Pan, Q. Huang, and Y. Shi, “Numerical analysis of unsteady hydrodynamic performance of pump-jet propulsor in oblique flow,” *Int. J. Nav. Archit. Ocean Eng.* **12**, 102–115 (2020).
- ⁵L. Lu, G. Pan, and P. K. Sahoo, “CFD prediction and simulation of a pump-jet propulsor,” *Int. J. Nav. Archit. Ocean Eng.* **8**, 110–116 (2016).
- ⁶H. Li, Q. Huang, G. Pan, and X. Dong, “Assessment of transition modeling for the unsteady performance of a pump-jet propulsor in model scale,” *Appl. Ocean Res.* **108**, 102537 (2021).
- ⁷Y. Shi, G. Pan, P. Wang, and X. Du, “Numerical simulation of cavitation characteristics of a pump-jet propeller,” *J. Shanghai Jiaotong Univ.* **48**(08), 1059–1064 (2014).
- ⁸G. Pan, L. Lu, and P. K. Sahoo, “Numerical simulation of unsteady cavitating flows of pump jet propulsor,” *Ship Offshore Struct.* **11**, 64–74 (2015).
- ⁹D. Qin, G. Pan, S. Lee, Q. Huang, and Y. Shi, “Underwater radiated noise reduction technology using sawtooth duct for pump jet propulsor,” *Ocean Eng.* **188**, 106228 (2019).
- ¹⁰Y. Sun, W. Liu, and T. Li, “Numerical investigation on noise reduction mechanism of serrated trailing edge installed on a pump-jet duct,” *Ocean Eng.* **191**, 106489 (2019).
- ¹¹H. Li, G. Pan, Q. Huang, and Y. Shi, “Numerical prediction of the pump-jet propulsor tip clearance vortex cavitation in uniform flow,” *J. Shanghai Jiaotong Univ.* **25**(3), 352–364 (2020).
- ¹²H. Li, Q. Huang, G. Pan, and X. Dong, “Wake instabilities of a pre-swirl stator pump-jet propulsor,” *Phys. Fluids* **33**, 085119 (2021).
- ¹³L. Wang, X. Lu, L. Wang, and M. Ling, “Propeller wake instabilities under turbulent-inflow conditions,” *Phys. Fluids* **34**, 085108 (2022).
- ¹⁴Q. Huang, H. Li, G. Pan, and X. Dong, “Effects of duct parameter on pump-jet propulsor unsteady hydrodynamic performance,” *Ocean Eng.* **221**, 108509 (2021).
- ¹⁵D. Qin, Q. Huang, G. Pan, P. Han, Y. Luo, and X. Dong, “Numerical simulation of vortex instabilities in the wake of a pre-swirl pump jet propulsor,” *Phys. Fluids* **33**, 055119 (2021).
- ¹⁶D. Qin, Q. Huang, Y. Shi, G. Pan, Y. Shi, and X. Dong, “Comparison of hydrodynamic performance and wake vortices of two typical types of pump jet propulsor,” *Ocean Eng.* **224**, 108700 (2021).
- ¹⁷Q. Huang, D. Qin, and G. Pan, “Numerical simulation of the wake dynamics of the pump jet propulsor in oblique inflow,” *Phys. Fluids* **34**, 065103 (2022).
- ¹⁸D. Qin, Q. Huang, G. Pan, P. Han, L. Chao, X. Luo, and P. Han, “Effect of the odd and even number of blades on the hydrodynamic performance of a pre-swirl pump jet propulsor,” *Phys. Fluids* **34**, 035120 (2022).
- ¹⁹L. Lu, G. Pan, J. Wei, and Y. Pan, “Numerical simulation of tip clearance impact on a pump jet propulsor,” *Int. J. Nav. Archit. Ocean Eng.* **8**, 219–227 (2016).
- ²⁰C. Qiu, Q. Huang, G. Pan, Y. Shi, and X. Dong, “Numerical simulation of hydrodynamic and cavitation performance of pump jet propulsor with different tip clearances in oblique flow,” *Ocean Eng.* **209**, 107285 (2020).
- ²¹H. Yu, Z. Zhang, and H. Hua, “Numerical investigation of tip clearance effects on propulsion performance and pressure fluctuation of a pump-jet propulsor,” *Ocean Eng.* **192**, 106500 (2019).
- ²²C. Wang, K. Weng, C. Guo, and L. Gu, “Prediction of hydrodynamic performance of pump propeller considering the effect of tip vortex,” *Ocean Eng.* **171**, 259–272 (2019).
- ²³C. Wang, K. Weng, C. Guo, X. Chang, and L. Gu, “Analysis of influence of duct geometrical parameters on pump jet propulsor hydrodynamic performance,” *J. Mar. Sci. Technol.* **25**, 640–657 (2020).
- ²⁴A. T. Shirazi, M. R. Nazari, and M. D. Manshadi, “Numerical and experimental investigation of the fluid flow on a full-scale pump jet thruster,” *Ocean Eng.* **182**, 527–539 (2019).
- ²⁵J. Gong, J. Ding, and L. Wang, “Propeller-duct interaction on the wake dynamics of a ducted propeller,” *Phys. Fluids* **33**, 074102 (2021).
- ²⁶S. Sun, C. Wang, C. Guo, and Y. Zhang, “Numerical study of scale effect on the wake dynamics of a propeller,” *Ocean Eng.* **196**, 106810 (2020).
- ²⁷M. Abdel-Maksoud and H. J. Heinke, “Scale effects on ducted propellers,” in *Proceedings of 24th Symposium on Naval Hydrodynamics*, Fukuoka, Japan (2002).

- ²⁸A. Bhattacharyya, V. Krasilnikov, and S. Steen, "A CFD-based scaling approach for ducted propellers," *Ocean Eng.* **123**, 116–130 (2016).
- ²⁹A. Bhattacharyya, V. Krasilnikov, and S. Steen, "Scale effects on open water characteristics of a controllable pitch propeller working within different duct designs," *Ocean Eng.* **112**, 226–242 (2016).
- ³⁰A. Bhattacharyya, V. Krasilnikov, and S. Steen, "Scale effects on a 4-bladed propeller operating in ducts of different design in open water," in Fourth International Symposium on Marine Propulsors (2015).
- ³¹J. K. Choi, H. G. Park, and H. T. Kim, "A numerical study of scale effects on performance of a tractor type podded propeller," *Int. J. Nav. Archit. Ocean Eng.* **6**, 380–391 (2014).
- ³²H. Yao and H. Zhang, "Numerical simulation of boundary-layer transition flow of a model propeller and the full-scale propeller for studying scale effects," *J. Mar. Sci. Technol.* **23**, 1004–1018 (2018).
- ³³Q. Yang, Y. Wang, and Z. Zhang, "Scale effects on propeller cavitating hydrodynamic and hydroacoustic performances with non-uniform inflow," *Chin. J. Mech. Eng.* **26**, 414–426 (2013).
- ³⁴A. Soydan and S. Bal, "An investigation of scale effects on marine propeller under cavitating and non-cavitating conditions," *Ship Technol. Res.* **68**, 166–178 (2021).
- ³⁵H. Li, Q. Huang, G. Pan, and X. Dong, "The scale effects on the open water performance of a pump-jet propulsor," *J. Mar. Sci. Technol.* **27**, 348–367 (2021).
- ³⁶J. Yang, D. Feng, L. Liu, X. Wang, and C. Yao, "Research on the performance of pump-jet propulsor of different scales," *J. Mar. Sci. Eng.* **10**, 78 (2022).
- ³⁷J. Lin, Y. Han, C. Guo, Y. Su, and R. Zhong, "Intelligent ship anti-rolling control system based on a deep deterministic policy gradient algorithm and the Magnus effect," *Phys. Fluids* **34**, 057102 (2022).
- ³⁸F. R. Menter, "Two-equation eddy-viscosity turbulence models for engineering applications," *AIAA J.* **32**(8), 1598–1605 (1994).
- ³⁹J. Baltazar, D. Rijpkema, J. Falcão de Campos, and J. Bosschers, "Prediction of the open-water performance of ducted propellers with a panel method," in Fifth International Symposium on Marine Propulsors (2018).
- ⁴⁰M. Ottersten, H. Yao, and L. Davidson, "Tonal noise of voluteless centrifugal fan generated by turbulence stemming from upstream inlet gap," *Phys. Fluids* **33**, 075110 (2021).
- ⁴¹I. B. Celik, U. Ghia, P. J. Roache *et al.*, "Procedure for estimation and reporting of uncertainty due to discretization in CFD applications," *J. Fluids Eng.* **7**, 130 (2008).
- ⁴²H. Zhang, J. Zang, D. Zhang, W. Shi, and J. Shen, "Analysis of the formation mechanism of secondary tip leakage vortex (S-TLV) in an axial flow pump," *Machines* **10**, 41 (2022).